catalysts

MDPI

Article

Engineering Noble Metal-like Bi onto Hierarchical $SrWO_4$ for the Enhancement of Photocatalytic Activity

Liang Tang, Jian Zhao, Xiao Wang, Jiajun Wang and Peng Zhang *

Key Laboratory of Organic Compound Pollution Control Engineering (MOE), School of Environmental and Chemical Engineering, Shanghai University, Shanghai 200444, China; tang1liang@shu.edu.cn (L.T.); zhaojian1997@shu.edu.cn (J.Z.); wangxiaowx@shu.edu.cn (X.W.); wangjiajun123@shu.edu.cn (J.W.)
* Correspondence: pengzhang@shu.edu.cn

Abstract: Solar-driven hydrogen production from water has attracted increasing attention due to sustainable H_2 fuel generation with zero-emissions. However, the design of a photocatalyst without noble metals to enable efficient water splitting is still critical for practical applications. In this study, the hierarchical microspheres of $SrWO_4$ assembled with well-defined metallic Bi nanoparticles were synthesized through mild hydrothermal aging. The resultant photocatalyst with optimum proportion exhibited the competitive performance of a high hydrogen-generation rate at 4.5 $mmol \cdot h^{-1} \cdot g^{-1}$, outperforming $SrWO_4$ and Bi by factors of 2.0 and 2.4, respectively. Both the experimental characterization and active analysis revealed that the synergistic effect of noble metal-like behavior of Bi and their electron-sink capacity mainly contribute to boosting the overall photocatalytic efficiency. This work may provide advanced insights into the application of economical bismuth elements as co-catalysts, instead of noble metals, to improve photocatalytic efficiency in solar-fuel conversion and environmental remediation.

Keywords: photocatalyst; hydrogen generation; bismuth metal; co-catalyst; synergistic effect

Citation: Tang, L.; Zhao, J.; Wang, X.; Wang, J.; Zhang, P. Engineering Noble Metal-like Bi onto Hierarchical SrWO4 for the Enhancement of Photocatalytic Activity. *Catalysts* **2022**, *12*, 787. https://doi.org/10.3390/catal12070787

Academic Editors: Vincenzo Vaiano and Giuseppina Luciani

Received: 30 May 2022
Accepted: 15 July 2022
Published: 18 July 2022

1. Introduction

With the worldwide consumption of fossil fuels in past decades, the major cause for concern has been increasingly concentrated on the long-lasting problem of greenhouse effect and serious environmental pollution [1,2], while the efficient solar-energy conversion from nanomaterials development has gradually become a major research topic to address the equilibrium between the reduction of human-energy usage and alleviating environmental issues [3–5]. As a promising alternative technology, semiconductor-based photocatalysis is being rapidly accelerated and extensively applied in the wide field of water splitting, environmental remediation, and photosynthesis [6–8]. Deriving from the prominent characteristics of their nontoxic nature, high chemical stability, and low cost, the prototype TiO_2 have been considered as efficient materials for this purpose of photocatalytic hydrogen-evolution reaction (HER) [9,10]. However, the sluggish reaction rate against their widespread use is mainly determined by the poor charge separation and relatively wide band gap [11]. Substantial efforts have been devoted to improving the total catalytic activity, including crystallinity, surface morphology, heterostructure construction, and heteroatom doping [12–17]. To date, the additional surface loading with a noble metal co-catalyst has been regarded as the most reliable strategy to improve their photocatalytic efficiency and stability [18]. However, high demand, as well as over-expenditure and scarcity significantly hinder their commercial development and scalable applications.

With respect to these precious metals, the promising candidate of bismuth (Bi) has attracted intense attention to exhibit their noble-metal-like behavior very recently. A variety of Bi coupled nanocomposites such as $Bi/(BiO)_2CO_3$ [19,20], Bi-BiOI [21], $Bi/g\text{-}C_3N_4$

[22], and Bi/$ZnWO_4$ [23] have been developed to perform their superior interfacial charge transfer kinetics and surface-reaction dynamics when competing with their individual phase. Indisputably, construction of strong metal-support interactions can profoundly influence the electronic structure and geometry of catalysts, which subsequently show a large impact on the catalytic performance [24,25]. Therefore, it is quite necessary to develop a new method to load the suitable co-catalysts on host species. To the best of our knowledge, a series of Bi-containing Titania with optimal structural regulation toward enhanced HER was widely studied in heterogeneous catalysis [26–31]. Binary metal oxides of AWO_4 (A = Ca, Sr, Ba) with scheelite structure have attracted extensive attention in recent years due to their importance in laser host materials for quantum electronics and medical applications, such as the prototype scintillator detectors of $CdWO_4$ and optical materials of $PbWO_4$ [32,33]. Furthermore, the body-centered tetrahedral structure of strontium tungstate ($SrWO_4$) has the physicochemical properties such as nontoxicity, light response, good electronic conductivity and thermal stability to compete with titanium dioxide, which was alternatively applied as optoelectronic material, optical fibers, photoluminescent medium, laser body, photocatalysts and antibacterial materials. While it is recognized as a representative non-titania inorganic candidate, its intrinsic catalysis for solar energy conversion is rarely studied [34–36]. However, the rare investigation on the effect of *s*-state occupation with cationic Bi on $SrWO_4$ has been considered, with particular emphasis on the structure–property relationship.

In this study, the photocatalytic HER of $SrWO_4$ was improved when in combination with the metallic Bi. The hydrogen production rate with respect to the global mass ratio has been determined and the continuous reactive capability was also monitored for long periods of time. It revealed that the hierarchical structure of $SrWO_4$ plays a critical role to promote the strong metal-support interaction deriving from the structural characteristics and spectral analysis. A significant mechanism during the heterogeneous catalysis was finally revealed to further realize their synergistic effect on contributing the decent stability, robust reactive sites, and efficient charge separation.

2. Results and Discussion

2.1. Structural Characterization

X-ray diffraction (XRD) patterns and Raman spectra of the resultant SWO and their composites of Bi/SWO-0.7 as well as the reference sample of pure Bi from direct synthesis are shown in Figure 1. It was found that the typical diffraction peaks of Bi/SWO-0.7 are all consistent with their corresponding standard cards of tetragonal SWO_4 (PDF#85-0587) and metal Bi (PDF#85-1331), indicating the successful heterostructure construction without any impurities (Figure 1a). When in comparison to their counterparts, the crystallinity of Bi/SWO-0.7 was not changed significantly after deposition of Bi metals on the surface because of their similar peak intensities and areas. As shown in the observed Raman spectra from 200 to 1100 cm^{-1}, there are five vibration modes of A_g (ν_1, 921 cm^{-1}), B_g (ν_3, 833 cm^{-1}), E_g (ν_3, 799 cm^{-1}), B_g (ν_4, 372 cm^{-1}), B_g (ν_2, 336 cm^{-1}) assigned to $SrWO_4$ (Figure 1b) [37]. Bi/SWO-0.7 maintained all prominent modes of $SrWO_4$ along with the slight negative shifting of A_g vibration ($[WO_4]^{2-}$ tetrahedron), indicating their strong interaction with metallic Bi (i.e., the *s*-state occupation) arising from their similar atomic radius of Bi (0.207 nm) and W (0.210 nm) [38]. When the mass ratio of Bi increased from 0.4 to 0.8, the intensity from vibrational mode of Bi-O bond lattice centered at 320 cm^{-1} was gradually increased against the pristine SWO (Figure S1a) [39]. Consistent with the result of increment of Bi intensity in XRD (Figure S1b), it is further proposed that there is a composition of $SrWO_4$ and mixed-sates of metallic Bi and Bi_2O_3 to construct the final product. However, no more characteristic peaks of oxidized Bi components appeared in XRD due to their low crystallinity.

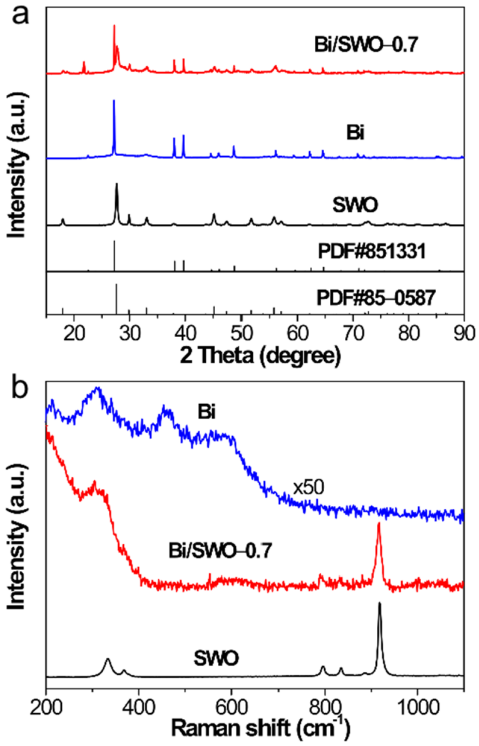

Figure 1. XRD patterns (**a**) and Raman spectra (**b**) of prepared Bi, SWO and Bi/SWO-0.7.

To elucidate the detailed oxidation states of Bi in Bi/SWO-0.7, X-ray photoelectron spectroscopy (XPS) was conducted (Figure 2). It was found that two main peaks centered around 157.08 eV and 162.35 eV are typically attributed to the Bi-Bi bonds of metallic Bi (Figure 2a), while the narrow Gauss-shaped symmetrical Bi $4f_{7/2}$ (158.96 eV) and Bi $4f_{5/2}$ (164.27 eV) core spectra are characteristic of the Bi^{3+} oxidation state in Bi_2O_3 [40,41]. According to the deconvoluted peaks of reference Bi, the discrete area ratio of metallic Bi to Bi^{3+} reflected the importance of the existence of host support during glucose-induced in-situ reduction in hydrothermal process [42]. Prior to Bi loading, the curve fitting in the O 1s region (Figure 2b) was attributed to lattice oxygen (530.37 eV) in $SrWO_4$ and adsorbed oxygen of OH^- or CO_3^{2-} (531.02 eV) on the surface. Additionally, the binding energies of Bi-O in Bi/SWO-0.7 and reference Bi are accordingly found to be 529.60 eV and 529.52 eV. However, the dramatic increment of oxide intensities was identified on reference Bi, suggesting that the richer metallic Bi predominantly formed on the surface of Bi/SWO-0.7 instead. The Sr $3d_{5/2}$ and Sr $3d_{3/2}$ orbitals of SWO are located at 133.15 eV and 134.91 eV (Figure 2c), while the W $4f_{7/2}$ and W $4f_{5/2}$ are located at 35.42 eV and 37.58 eV (Figure 2d), respectively. It can be seen that both spin orbitals of Sr 3d (132.77 eV and 134.53 eV) and W 4f (34.87 eV and 37.02 eV) for Bi/SWO-0.7 are both negatively shifted to the lower binding energies, attributed to the stereochemical activity of s orbitals through the feasible interfacial electron transfer between the $6s^2$ lone-pair electrons of Bi and the $[WO_4]^{2-}$ tetrahedron [43]. All these results confirmed that the Bi/SWO-0.7 heterostructure was successfully prepared, as well as the strong interaction between the metallic Bi and $SrWO_4$.

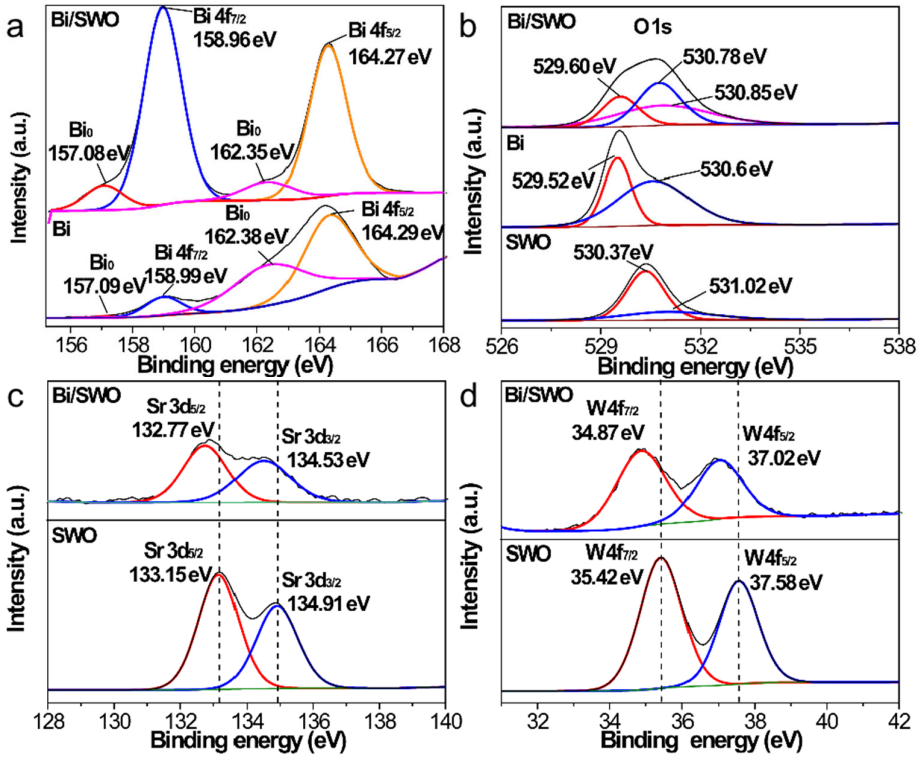

Figure 2. High-resolution XPS spectra of Bi 4f (**a**), O 1s (**b**), Sr 3d (**c**), and W 4f (**d**) for Bi, SWO and Bi/SWO-0.7.

The typical morphology of the hierarchical structure was investigated by scanning electron microscopy (SEM). When compared to original SWO (Figure 3a), Bi/SWO-0.7 products maintained the well-dispersed spherical-shape morphology in the average diameters of ~10 μm along with a rougher surface (Figure 3b). Determined from the higher magnification image (insert in Figure 3b), we also observed that Bi/SWO-0.7 with porous structures was assembled with radial alignment of a worm-like host structure (Figure S2a). Their porosity was furthered to verify from surface areas and average pore diameters of N_2 adsorption-desorption isotherms (Figure S3). It was found that the specific surface area of Bi/SWO-0.7 (24.9 $m^2 g^{-1}$) is significantly higher than that of the counterpart SWO (13.7 $m^2 g^{-1}$), which is possibly due to the more regular nanoparticle arrangement of pores in the structures as the gradual increment of Bi (Table S1), while Bi/SWO-0.8 does not have this feature because of the pore structures filled by the overloading of Bi particles. In contrast, the pore size distribution of Bi/SWO-0.7 shows the unique micropore type that coincides with the characteristics of their hierarchical porous structure from SEM (insert in Figure S3). Interestingly, all the Sr, W, and O signals exhibited the microsphere morphology from the recorded elemental mapping (Figure 3c), whereas Bi species uniformly distributed on the surface of the host microstructure instead of the particles aggregation from counterpart Bi (Figure S2b). The energy dispersive spectrum (EDS) shows that Bi/SWO-0.7 is composed of 33.95, 14.52, 37.38, and 14.15 wt% Bi, Sr, W and O respectively without any impurities (Figure S4 and Table S2). While the higher molar ratio of Sr to O (1:5.1) than that of $SrWO_4$ (1:4) indicated the existence of oxide species of Bi on the surface, this results in a bit smaller molar ratio of Bi than the well matched XPS analysis (70.8%) in relation to experimental composition (70.0%).

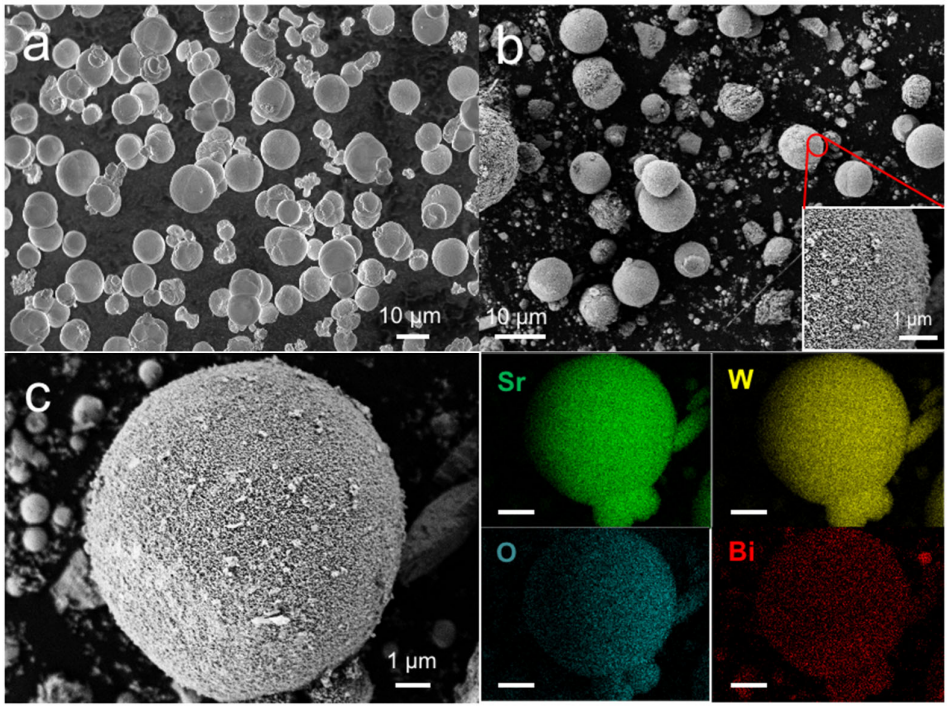

Figure 3. SEM images of SWO (**a**) Bi/SWO-0.7 (**b**) and the elemental mapping analysis (**c**). The inset of panel (**b**) is the magnified image.

2.2. Growth Mechanism

It is believed that the photocatalysts with novel structures always possess the unique physicochemical properties [36]. Previous studies have shown that the growth mechanism and shape evolution process of uniform Bi particles assigned on porous host of SWO should be systematically investigated. As a monosaccharide sugar, glucose can work as the mild reducing agent arising from the positive result for Fehling's test [44]. When the reductive glucose was introduced into the Bi precursors, the irregular aggregations assembled with dense Bi particles were formed after the *in-situ* reduction of Bi^{3+} species in hydrothermal aging (upper route in Figure 4). For comparison, the hierarchical microspheres of SWO as the composite substrate were added to obviously alter the final morphology attributed to the bifunctional roles of glucose as both surfactant and reductant [43]. In this case, the capping activity of glucose is expected to play the critical role to successfully prevent the structural aggregation through the sequential pathway (bottom route in Figure 4). First, the oxygen atoms in carbonyl and hydroxyl groups of glucose would form the hydrogen bonds with surface hydroxyls of SWO, resulting in glucose molecules completely entwined in the interspace of the backbone. Subsequently, trivalent metal cations electrostatically adsorbed on the polar headgroup of glucose, which acted as molecular ligand and micelles constructor to bridge with SWO [45]. Finally, the glucose with high steric hindrance effect was moderately increased to reduce Bi^{3+} to metallic Bi for uniformly wrapping on SWO surface as active sites, leading to agglomeration prevention during the hydrothermal heating. To extract information of electrostatic effect on the underlying glucose-assistant anisotropic growth, the pH independent morphology of the control products was taken, even with glucose addition. It is evident that the pH variation as well as with additive glucose has negligible effect on the supporting structure of SWO (Figures S5 and S6). Based on these results, it can be concluded that both glucose capped synthesis and hierarchical backbone are crucial for the uniform coverage of Bi particles under the mild condition (pH~6.9).

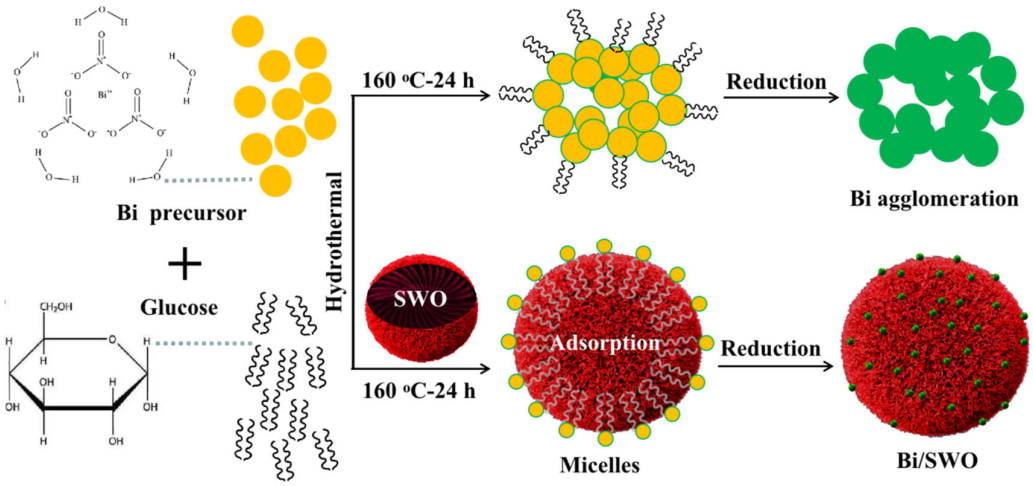

Figure 4. Schematic illustration for the glucose-assistant growth mechanism of Bi/SWO.

2.3. Charge Separation

To better understand the influence of strong metal-support interaction on interfacial electron transfer, the photoelectrochemical performance was characterized using *I–t* curves, and subsequently impedance spectra (EIS) measurements. Bi/SWO-0.7 showed remarkable increment and stable photocurrent density up to 42.9 nA cm^{-2} (Figure 5a) upon light illumination, which is approximately 2.4 and 10.1 times larger than that of SWO (17.9 nA cm^{-2}) and Bi (3.9 nA cm^{-2}), respectively. In accordance with the result of transient photocurrent response, Bi/SWO-0.7 with the most reduced semi-diameter of the semicircle radius represented a minimum charge transfer resistance compared to individual component (Figure 5b). It is well known that the relative intensity of photoluminescence (PL) emission is directly proportional to the recombination rate of photoinduced electron and hole. When in comparison to the PL emission of pure SWO, ranged from UV to visible light regions, the Bi/SWO composites show a sharply diminished PL intensity, which supposes the prominent contribution of the Bi element on the apparent descent of the recombination rate (Figure S7) [46]. It was obviously observed that metallic Bi loading with the optimal amount displays the lowest intensity significantly, reflects its superior capability of charge separation. In contrast, the characteristics of interfacial charge transfer on Bi/SWO-0.7 were further investigated through the single-particle PL measurements (Figure 5c inset). Matched well with the preceding results of a broad steady-state emission (inset), it revealed the longer average lifetime (τ_{PL}) of photo-induced electron of Bi/SWO-0.7 (3.68 ns) than that of SWO (2.20 ns) through the transient PL spectra (Figure 5d). Since the emitting sites on the surface were complicated beyond the instrumental resolution, the spatial distribution of active sites assigned to elemental Bi are not clear here for analysis. In summary, all results supported the fact that metallic Bi intimately coupled with SWO can serve as electron traps, which significantly facilitates charge separation and subsequent HER kinetics toward high hydrogen production [47].

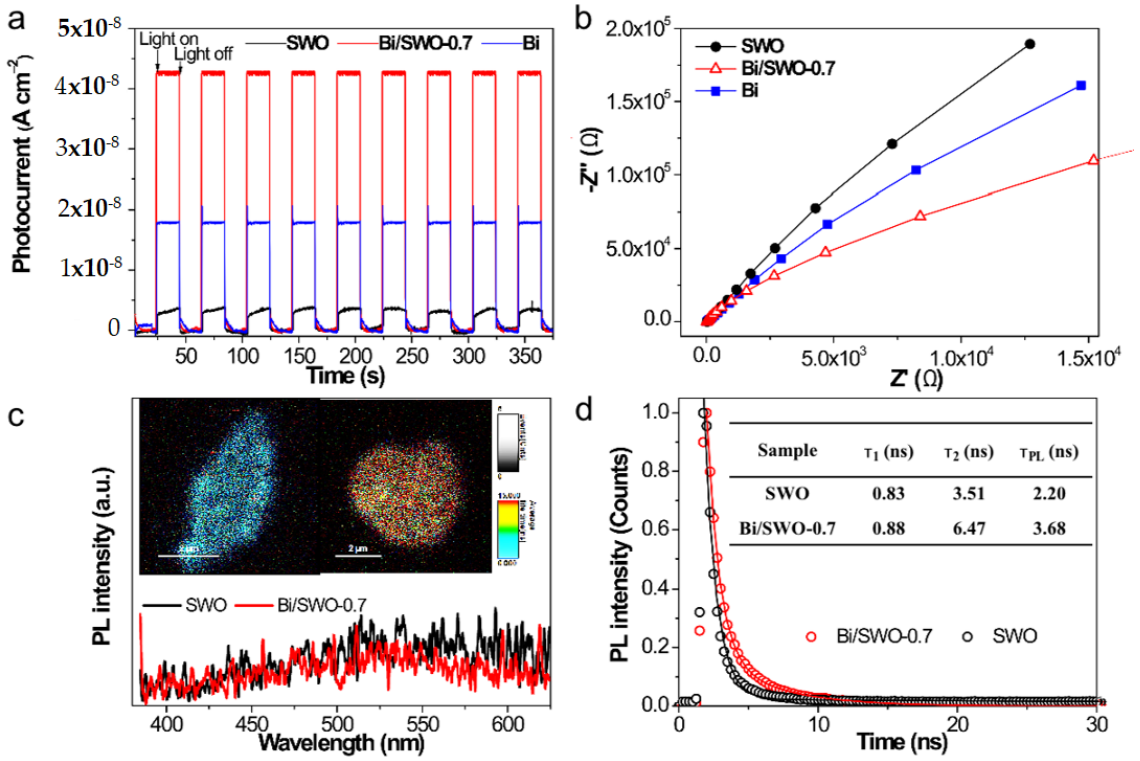

Sample	τ_1 (ns)	τ_2 (ns)	τ_{PL} (ns)
SWO	0.83	3.51	2.20
Bi/SWO-0.7	0.88	6.47	3.68

Figure 5. Transient photocurrent response (**a**) and electrochemical impedance spectra (**b**) of Bi, SWO and Bi/SWO-0.7. The single-particle PL images (inset) and PL spectra (**c**), and the time-resolved fluorescence decay spectra (**d**) between SWO and Bi/SWO-0.7. The solid curves indicate the multi-exponential curves fitted to the kinetic traces using biexponential decay function.[-8]

2.4. Photocatalytic Hydrogen Production Activities

Photocatalytic hydrogen production over catalysts was tested in the presence of an electron donor (Na_2S-Na_2SO_3) under irradiation with a mercury lamp (Figure 6). The results showed that a promising improvement of photocatalytic activity after Bi loading on SWO (Bi/SWO) was observed when compared to both individual SWO (2346.8 μmol·g^{-1}·h^{-1}) and pure Bi (1925.1 μmol·g^{-1}·h^{-1}). It was found that the reactive rate gradually increased when the loading ratio was less than 0.7 due to an increase in the number of active sites from Bi (Figure S8). However, an excessive loading ratio, more than 0.7, lowered the total efficiency, possibly suffering from the obstructive light absorption and interfacial barrier from serious agglomeration of the Bi covering (Figure S8) [48]. The fact that the optimal Bi/SWO-0.7 with maximum active sites produced the highest amount of hydrogen around 13,634.3 μmol·g^{-1} after 3 h (Figure 6a) strongly revealed the crucial interaction between Bi and SWO for catalytic promotion. In particular, it is noted that the visible performance of Bi/SWO-0.7 is negligible, despite its absorption spectral profile extended from an intrinsic absorption edge of SWO (~400 nm) to the visible light and near-infrared regions (Figure S9a), which corresponds to the narrowed bandgap from 3.25 eV to 4.47 eV via Tauc plots analysis (inset in Figure S9a). To our knowledge, this phenomenon is not consistent with the direct photocatalytic behavior of plasmonic Bi, mainly attributed to the insufficient charge generation from their poor incident light excitation at the resonance wavelength [17]. Additionally, the influence of the surface area on the photoactivity seems to be also insignificant because of their close S_{BET} (Table S1). All the above results indicated that Bi/SWO-0.7 with competitive activity should be most efficient in spatial charge separation, as a result of the structural modification with Bi.

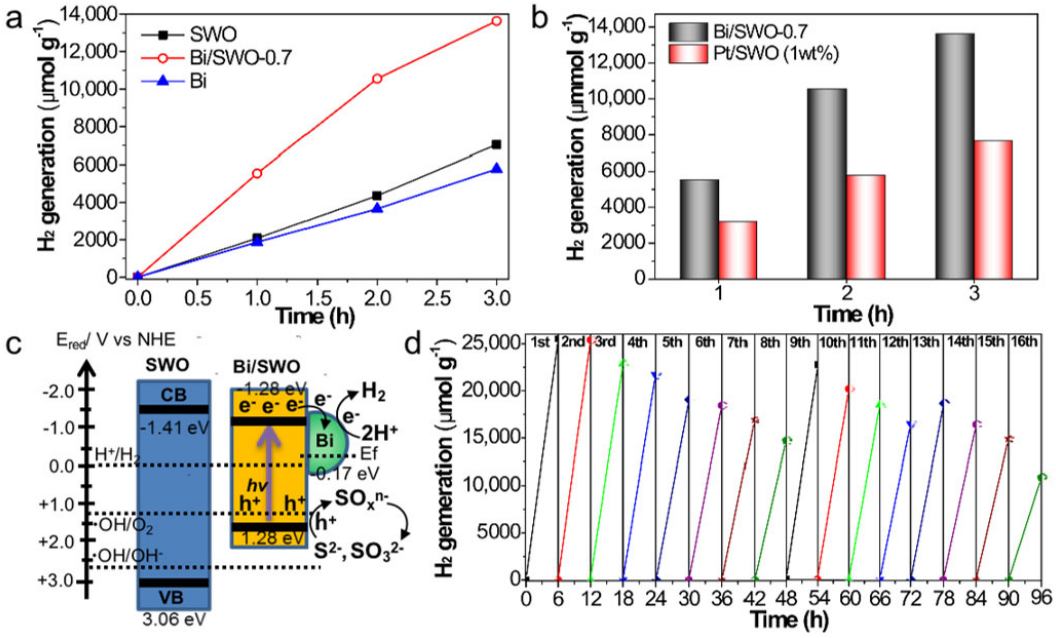

Figure 6. Hydrogen generation over the different catalyst (**a**) and their competitive activity with Pt loading (**b**). Recycled hydrogen evolution measurement (**c**) and proposed photocatalysis mechanism (**d**).

2.5. Photocatalysis Mechanism and Stability

With respect to its commercial application, photocatalytic hydrogen generation from platinum (1 wt%) photodeposited SWO (Pt/SWO) was measured for a typical comparison. Note that Bi/SWO-0.7 exhibited a higher activity (13634.3 μmol·g^{-1}) than Pt/SWO (7658.6 μmol·g^{-1}) under the same conditions (Figure 6b), further indicating the alternative competitor of Bi endowed with noble metal-like behavior. In this case, a schematic illustration of the band alignment within Bi/SWO-0.7 for mechanistic promotion of photocatalytic performance was shown in Figure 6c. The band positions could be calculated based on the bandgap values and valence-band XPS (VB-XPS) data (Figure S9b), while their strong interaction in hybridized charge migration and weak plasmonic effect would give rise to the reconstruction of the negative states in relation to pristine SWO. Upon light illumination on Bi/SWO-0.7, the SWO is excited to generate charge pairs of electrons (e^-) and holes (h^+) in the conduction (CB) and valence bands (VB), respectively. Furthermore, electrons escaped from geminate recombination and exergonically relaxed into the neighbor electron-sink of Bi nanoparticles (Fermi energy = −0.17 eV) from the higher energies CB (−1.28 eV) of Bi/SWO. Consequently, holes mostly accumulated on the surface of Bi/SWO, while electrons accumulated on Bi. After that, the accumulated electrons on dispersive Bi centers subsequently reduced the proton (H^+) to generate H_2, inferring their resembling feature as the noble metals to accelerate interfacial charge transfer for suppressing the back recombination with retentive holes. Meanwhile, substantial holes at the VB of Bi/SWO (1.28 eV) are scavenged preferably by sacrificial S^{2-}–SO_3^{2-} anions (0.17 V vs. NHE) rather than water oxidation (1.23 V vs. NHE) through the polysulfide S_n^{2-}–based mediation of redox events [49]. Therefore, it can be reasonably inferred that the promising performance of Bi/SWO-0.7 stems from the synergistic interaction between well-aligned Bi exposure and porous 3D supports for significant promotion of charge separation and mass transfer, thereby ensuring the unique structure–property relationship in the heterogeneous system.

As well as high photocatalytic activity, a good photocatalyst should display critical stability. The repeated experiment of Bi/SWO-0.7 was tested by running the photocatalytic reaction for 96 h (Figure 6d). It was clearly observed that the photocatalytic efficiency is

mainly stable, and gradually drops within the first eight recycles. After replenishing the catalysts' amounts (50 mg) in fresh sacrificial reagents, the activity was recovered at the ninth cycle, further excluding the effect of mass missing from multiple treatments of centrifugation and washing in each cycle. Although the loss of activity that occurred at 96 h was significant, the reusability in the continuous eight recycles (9th–16th) seems a step closer to the former case (1st–8th), which confirms their comparable stability. The few changes in crystallographic structure were also observed by comparing the characteristic peaks of XRD on Bi/SWO-0.7 before and after reaction (Figure S10). However, was discovered that some host structures were collapsed (Figure S11), resulting in the irregular agglomeration of Bi particles after leaching from preliminary support. This result further indicates that such structural photocorrosion may be considered as the possible cause of their gradual decrement of activity after long-term reactions.

It is well known that photocatalytic water splitting consists of proton reduction coupled to sluggish water oxidation. The fact that concurrent reactions of electrons and holes with preferable potential on photoexcited catalysts can spontaneously participate in the redox activation of suitable reactants [50]. The oxidative capability of photocatalysts was evaluated by performing the aerobic degradation of tetracycline (TC), benzyl alcohol (BP), phenol (Ph) and 4-chlorophenol (4-CP). In comparison to the 61% removal of BP after 1 h, the Bi/SWO-0.7 performed nearly 100% degradation of TC, Ph and 4-CP within 30 min (Figure S12a). It can be reasonably inferred that the efficient pollutant degradation and TOC (41.3~80.4%) removal stem from the direct oxidation of the holes (inset in Figure S12a). One consideration of less expensive sacrificial reagents, from the viewpoint of industrial application, is that it is favorable if the anaerobic photodegradation is coincidental with the typical operations of hydrogen production when pollutants serve as electron donors. Therefore, the hydrogen production activities with additive organic pollutants were further investigated in the identical system. Concurrently with complete degradation of TC (TOC, 80.4%), Bi/SWO-0.7 displays a significantly enhanced hydrogen production rate up to 7207.9 from 4544.8 $\mu mol \cdot g^{-1} \cdot h^{-1}$ (Figure S12b), evidently demonstrating their synergistic effect on the promotion of catalytic performance. However, as they suffer from an unstable structure, as shown in our present work, it would be of great interest to construct the potential heterojunction for our future study in the field of redox-coupled pollutant degradation and hydrogen production [51].

3. Materials and Methods

3.1. Chemical Reagents

All chemicals were analytical grade or higher: sodium tungstate, bismuth nitrate pentahydrate, glucose, sodium sulfide nonahydrate, sodium sulfite were all purchased from Adamas (Shanghai, China). Strontium nitrate was purchased from Aladdin (Shanghai, China). All raw materials were analytical reagents and were used without further purification.

3.2. Characterization

Powder X-ray diffraction (XRD) patterns were recorded on a Bruker D8 Advance X-ray diffractometer with Cu Kα (λ = 0.15406 nm). The Raman spectra was tested via the Raman spectrometer (Renishaw inVia Raman Microscope, laser wavelength was 785 nm, laser power was 5%, exposure time was 10 s, integration times was 3). The morphology of the materials was observed by scanning electron microscopy (SEM, Gemini SEM 300) equipped with energy dispersive X-ray spectroscopy (EDS). X-ray photoelectron spectra (XPS) and valence-band X-ray photoelectron spectra (VB-XPS) were obtained by a Thermo Scientific K-Alpha. UV-visible diffused reflectance spectroscopy (DRS) was obtained using a UV-visible spectrophotometer (UV-2600, Shimadzu, Japan). Photoluminescence (PL) spectra were recorded using a Gangdong F-320 spectrometer using 275 nm as the excitation wavelength. The Brunauer–Emmett–Teller (BET) surface area was measured using a

nitrogen adsorption instrument (Micromeritics ASAP 2460 analyzer) at liquid-nitrogen temperature. The specific surface areas of samples were determined by the Brunauer–Emmett–Teller (BET) method, and the pore size distribution and pore volume of samples were calculated by the Barrette–Joynere–Halenda (BJH) method.

3.3. Synthesis of Photocatalyst

In a typical procedure for direct synthesis of the $SrWO_4$ (SWO) microstructure [52], the source materials of $Sr(NO_3)_2$ and Na_2WO_4 with equimolar quantities of 5 mmol were separately dissolved in 25 mL distilled water at room temperature. Then the Na_2WO_4 aqueous solution was slowly added into the $Sr(NO_3)_2$ solution without stirring or shaking followed by the pH adjudication from H_2SO_4 and NaOH solution. Immediately, white precipitates appeared and were maintained for 2 h at room temperature. Finally, the SWO products were collected after drying at 70 °C for 5 h, followed by washing with water several times. After SWO formation, we prepared the hierarchical composites of Bi/SWO through the hydrothermal method [23]. First, 1 mmol of Bi $(NO_3)_3{\cdot}5H_2O$ and 1 mmol of glucose were mixed in 30 mL of ethylene glycol under continuous stirring. After the mixture was dissolved completely, a certain amount of SWO powder was added and dispersed ultrasonically. Then, the final suspensions were transferred into a 50 mL Teflon-lined autoclave reactor and heated at 160 °C for 24 h. After cooling down to room temperature, the precipitates were collected, followed by washing with ethanol and deionized water, and drying at 70 °C for 4 h. For ease and clarity, the synthesized Bi/SWO composites were denoted as Bi/SWO-x, where x represents the different mass ratio of Bi among 0.4, 0.5, 0.6, 0.7 and 0.8, respectively. For comparison, Bi nanoparticles were prepared under the identical conditions with addition of $Bi(NO_3)_3$ as precursors.

3.4. Photocatalytic Hydrogen Evolution Reaction

The photocatalytic hydrogen-evolution reaction was conducted in an all-glass automatic on-line trace gas analysis system (Beijing China Education AuLight Technology Co., Ltd., Beijing, China) connected to a fully automatic flow control gas chromatograph (GC-CEAuLight, Beijing, China) with a thermal conductivity detector (TCD). Typically, 50 mg of the photocatalyst was dispersed into a 100 mL aqueous solution with a sacrificial agent (0.35 M $Na_2S{\cdot}9H_2O$ and 0.25 M anhydrous Na_2SO_3). The entire system was degassed several times before the reaction to remove the air from the system. Under the irradiation of Hg lamp (250 W, Shanghai Jiguang Special Lighting Electric Appliance Factory, Shanghai, China), the generated hydrogen in this reactor was analyzed by online GC (CEAuLight) after every time interval. Finally, the samples were collected after centrifugation and washing for the recycling experiment. The reusability test was carried out 16 times and then each reaction lasted for 6 h per cycle. During the reaction, the temperature of the entire circulation system was maintained at 293 K by using a cooling circulation water system.

3.5. Photoelectrochemical Measurements

Electrochemical impedance spectroscopy (EIS) and Mott-Schottky (MS) analysis were performed on a three-electrode potentiostat (CHI660E, Shanghai, China) with an electrolyte of 0.5 M Na_2SO_4 solution. A platinum, Ag/AgCl electrode, and the conductive ITO glass coated with photocatalysts were used as the counter, reference, and working electrodes. EIS tests were carried out in the frequency range of 10-1 and 102 Hz. MS tests were carried out using the impedance-potential model over a voltage range of -1 to 1 V at a frequency of 1 kHz. Current-time curves (I-t) were determined at 0 V versus Ag/AgCl in Na_2SO_4 (0.5 M) at ambient temperature using a 300 W Xe lamp (Perfect Light MICROSOLAR 300, Beijing, China) with a UV cut-off filter ($\lambda > 400$ nm).

3.6. Sample Preparation for Single-Particle PL Experiments

The quartz cover glasses were purchased from Matsunami Glass and cleaned by sonication in a 20% detergent solution (Cleanace, As One) for 6 h, followed by washing with warm water for 5 times. Finally, the quartz cover glasses were washed again with Milli-Q ultrapure water (Millipore). The suspension with a low concentration of different samples was spin-coated on the pre-cleaned quartz cover glass, which was subsequently annealed at 100 °C for 0.5 h to immobilize the particles on the glass surface.

3.7. Single-Particle Pl Measurements by Confocal Microscopy

Single-particle PL images and spectra were recorded by using an objective scanning confocal fluorescence microscope system (PicoQuant, MicroTime 200). The samples were excited through an oil-immersion objective lens (Olympus, UplanSApochromat, 100×, 1.4 NA) with a circular-polarized 375-nm pulsed laser (Spectra-Physics, Mai Tai HTS-W with an automated frequency doubler, Inspire Blue FAST-W; 0.8MHz repetition rate) controlled by a PDL-800B driver (PicoQuant). The emission from the sample was collected by the same objective and detected by a single-photon avalanche photodiode (Micro Photon Devices, PDM 50CT) through a dichroic beam splitter (Chroma, z405rdc) and long pass filter (Chroma, HQ435CP). For the spectroscopy, only the emission that passed through a slit was detected with the imaging spectrograph (Acton Research, SP-2356) equipped with an electronmultiplying charge-coupled device (EMCCD) camera (Princeton Instruments, ProEM).

4. Conclusions

In summary, the appropriate amount of metallic Bi particles was successfully assigned on SWO microspheres through the glucose-assistant one-pot hydrothermal method. In comparison to individual $SrWO_4$ (2.3 $mmol \cdot h^{-1} \cdot g^{-1}$) and Bi (1.9 $mmol \cdot h^{-1} \cdot g^{-1}$), the Bi/SWO greatly enhanced the reactive rate of HER up to 4.5 $mmol \cdot h^{-1} \cdot g^{-1}$ to reveal the synergistic contribution of strong metal-support interactions. The representative electron-sink-capacity of Bi on SWO contributed twice as much activity than Pt/SWO, leading to their potential application as noble-metal-alternative co-catalysts. The remarkable increment of photocurrent around 42.9 nA cm^{-2} and the smallest semicircle radius through the electrochemical analysis, as well as the longer average lifetime of 3.68 ns in fluorescence decay, evidently reflected their superior capability of charge separation compared to that of the pure phase. When coupling the methodology of glucose encapsulated metallic loading with 3D host structures, this work could provide a new insight into the structure-activity relationships for collaboratively promoting the photocatalytic performance of $SrWO_4$-based materials in hydrogen production and even organic pollutant degradation.

Supplementary Materials: The following supporting information can be downloaded at: www.mdpi.com/article/10.3390/catal12070787/s1, Figure S1: Raman spectra (a) and XRD patterns (b) of SWO with different mass ratio of Bi; Figure S2: SEM images of SWO after hydrothermal treatment (a) and direct synthesis of Bi (b); Figure S3: N_2 adsorption–desorption isotherms curves and pore diameter distribution curves (inset) of Bi, SWO and Bi/SWO-0.7, respectively; Figure S4: EDX spectrum of the resultant Bi/SWO-0.7; Figure S5: SEM images of pH independent morphology on the control products along with glucose addition; Figure S6: XRD patterns of SWO samples obtained with and without glucose addition from hydrothermal aging at pH = 6.9; Figure S7: PL spectra for SWO and their composites with different amounts of Bi; Figure S8: Comparable H_2 generation between SWO and their composites with different amounts of Bi; Figure S9: Steady-state diffuse reflectance UV-visible spectrum (a) with corresponding Tauc plots (inset) and valence-band XPS (b) for the samples; Figure S10: The comparable XRD patterns of Bi/SWO-0.7 before and after long-term experiment; Figure S11: The SEM images of Bi/SWO-0.7 after long-term experiment; Figure S12: Photodegradation of typical pollutants (a) with their total organic carbon (TOC) removal (inset) and synchronical H_2 production and TC degradation (b). Table S1: The specific surface area and the average pore size of the photocatalysts; Table S2: Elemental composition of Bi/SWO-0.7 from XPS and EDS.

Author Contributions: Conceptualization, Methodology, Formal analysis, Investigation, Writing–original and draft, L.T.; Investigation, Methodology, Formal analysis, Data curation, Writing–original & draft, Validation, Writing–review and editing, J.Z.; Investigation, Writing–review and editing, X.W.; Data curation, J.W.; Data curation, Methodology, Conceptualization, Investigation, Supervision, Writing–review & editing, Project administration, P.Z. All authors have read and agreed to the published version of the manuscript.

Funding: This research was funded by the National Natural Science Foundation of China (42107416) and the Program for Professor of Special Appointment (Eastern Scholar) at Shanghai Institutions of Higher Learning (TP2019040).

Acknowledgments: We are grateful to Zaizhu Lou, Jinan University, for technical assistance on the single-particle PL measurement.

Conflicts of Interest: The authors declare no conflict of interest.

References

1. Cheng, Y.C.; Yang, G.S.; Jiang, H.R.; Zhao, S.L.; Liu, Q.Y.; Xie, Y.S. Organic sensitizers with extended conjugation frameworks as cosensitizers of porphyrins for developing efficient dye-sensitized solar cells. *ACS Appl. Mater. Inter*. **2018**, *10*, 38880–38891.
2. Ma, Y.X.; Yin, L.S.; Cao, G.J.; Huang, Q.L.; He, M.S.; Wei, W.X.; Zhao, H.; Zhang, D.E.; Wang, M.Y.; Yang, T. Pt-Pd bimetal popcorn nanocrystals: Enhancing the catalytic performance by combination effect of stable multipetals nanostructure and highly accessible active sites. *Small* **2018**, *14*, 1703613.
3. Wang, Y.M.; Wei, W.; Liu, X.; Gu, Y.J. Research progress on polymer heterojunction solar cells. *Sol. Energy Mater. Sol. Cells*. **2012**, *98*, 129–145.
4. Li, P.S.; Duan,X. X.; Kuang, Y.; Li, Y.P.; Zhang, G.X.; Liu, W.; Sun, X.M. Tuning electronic structure of NiFe layered double hydroxides with vanadium doping toward high efficient electrocatalytic water oxidation. *Adv. Energy Mater*. **2018**, *8*, 1703341.
5. Hang, L.F.; Zhang, T.; Sun, Y.Q.; Men, D.D.; Lu, X.J.; Zhang, Q.L.; Cai, W.P.; Li, Y. $Ni_{0.33}Co_{0.67}MoS_4$ nanosheets as a bifunctional electrolytic water catalyst for overall water splitting. *J. Mater. Chem. A* **2018**, *6*, 19555–19562.
6. Yan, H.J.; Yang, J.H.; Ma, G.J.; Wu, G.P.; Zong, X.; Lei, Z.B.; Shi, J.Y.; Li, C. Visible-light-driven hydrogen production with extremely high quantum efficiency on Pt–PdS/CdS photocatalyst. *J. Catal*. **2009**, *266*, 165–168.
7. Xiang, Q.J.; Yu, J.G.; Jaroniec, M. Graphene-based semiconductor photocatalysts. *Chem. Soc. Rev.* **2012**, *41*, 782–796.
8. Liu, G.; Yu, J.C.; Lu, G.Q.; Cheng, H.M. Crystal facet engineering of semiconductor photocatalysts: Motivations, advances and unique properties. *Chem. Commun*. **2011**, *47*, 6763–6783.
9. Anucha, C.B.; Bacaksiz, E.; Stathopoulos, V.N.; Pandis, P.K.; Argirusis, C.; Andreouli, C.D.; Tatoudi, Z.; Altin, I. Preparation and Characterization of Supported Molybdenum Doped TiO_2 on α-Al_2O_3 Ceramic Substrate for the Photocatalytic Degradation of Ibuprofen (IBU) under UV Irradiation. *Catalysts* **2022**, *12*, 562.
10. Zhang, Y.; Miao, B.; Chen, Q.; Bai, Z.; Cao, Y.; Davaa, B. Synthesis, Structure, and Photocatalytic Activity of TiO2-Montmorillonite Composites. *Catalysts* **2022**, *12*, 486.
11. Li, X.; Yu, J.; Low, J.; Fang, Y.; Xiao, J.; Chen, X. Engineering heterogeneous semiconductors for solar water splitting. *J. Mater. Chem. A* **2015**, *3*, 32485–32534.
12. Xiong, T.; Cen, W.L.; Dong, F.; Zhang, Y.X.; Bridging the g-C_3N_4 interlayers for enhanced photocatalysis, *ACS Catal.* **2016**, *6*, 2462–2472.
13. Pikuda, O.; Garlisi, C.; Palmisano, G.; Scandura, G.; Micro-mesoporous N-doped brookite-rutile TiO_2 as efficient catalysts for water remediation under UV-free visible LED radiation. *J. Catal*. **2017**, *346*, 109–116.
14. Wen, J.Q.; Xie, J.; Yang, Z.H.; Shen, R.C.; Li, H.Y.; Luo, X.Y.; Chen, X.B.; Li, X. Fabricating the robust g-C_3N_4 nanosheets/carbons/NiS multiple heterojunctions for enhanced photocatalytic H_2 generation: An insight into the trifunctional roles of nanocarbons. *ACS Sustain. Chem. Eng*. **2017**, *5*, 2224–2236.
15. He, W.J.; Sun, Y.J.; Jiang, G.M.; Li, Y.H.; Zhang, X.M.; Zhang, Y.X.; Zhou, Y.; Dong, F. Defective Bi_4MoO_9/Bi metal core/shell heterostructure: Enhanced visible light photocatalysis and reaction mechanism. *Appl. Catal. B Environ*. **2018**, *239*, 619–627.
16. Yang, J.; Jiang, P.F.; Yue, M.F.; Yang, D.F.; Cong, R.H.; Gao, W.L.; Yang, T.J. $Bi_2Ga_4O_9$: An undoped single-phase photocatalyst for overall water splitting under visible light. *J. Catal*. **2017**, *345*, 236–244.
17. Zhang, G.G.; Lan, Z.A.; Wang, X.C. Conjugated polymers: Catalysts for photocatalytic hydrogen evolution. *Angew. Chem. Int. Ed*. **2016**, *55*, 15712–15727.
18. Zhang, G.G.; Lan, Z.A.; Lin, L.H.S.; Wang, X.C.; Overall water splitting by Pt/gC_3N_4 photocatalysts without using sacrificial agents. *Chem. Sci*. **2016**, *7*, 3062–3066.
19. Dong, F.; Li, Q.Y.; Sun, Y.J.; Ho, W.K. Noble metal-like behavior of plasmonic Bi particles as a cocatalyst deposited on $(BiO)_2CO_3$ microspheres for efficient visible light photocatalysis. *ACS Catal*. **2014**, *4*, 4341−4350.
20. Xiong, T.; Dong, A.H.; Huang, W.; Cen, W.L.; Zhang, Y.X.; Dong, F. Single precursor mediated-synthesis of Bi semimetal deposited N-doped $(BiO)_2CO_3$ superstructures for highly promoted photocatalysis. *ACS Sustain. Chem. Eng*. **2016**, *4*, 2969–2979.
21. Chang, C.; Zhu, L.Y.; Fu, Y.; Chu, X.L. Highly active Bi/BiOI composite synthesized by one-step reaction and its capacity to degrade bisphenol A under simulated solar light irradiation. *Chem. Eng. J*. **2013**, *233*, 305−314.

22. Dong, F.; Zhao, Z.W.; Sun, Y.J.; Zhang, Y.X.; Yan, S.; Wu, Z.B.; An advanced semimetal–organic Bi spheres–g-C_3N_4 nanohybrid with SPR-enhanced visible-light photocatalytic performance for NO purification. *Environ. Sci. Technol*. **2015**, *49*, 12432–12440.
23. Gao, Y.X.; Huang, Y.; Li, Y.; Zhang, Q.; Cao, J.J.; Ho, W.K.; Lee, S.C. Plasmonic Bi/$ZnWO_4$ microspheres with improved photocatalytic activity on NO removal under visible light. *ACS Sustain. Chem. Eng*. **2016**, *4*, 6912–6920.
24. Zhang, J.; Zhu, D.Z.; Yang, J.F.; Wang, C.A. Strong metal-support interactions induced by an ultrafast laser. *Nat. Commun*. **2021**, *12*, 6665.
25. Du, H.; Liu, Y.N.; Shen, C.C.; Xu, A.W. Nanoheterostructured photocatalysts for improving photocatalytic hydrogen production. *Chin. J. Catal*. **2017**, *38*, 1295–1306.
26. Solís, M.; Rincón, M.E.; Calva, J.C.; Alvarado, G.; Bismuth sulfide sensitized TiO_2 arrays for photovoltaic applications. *Electrochim. Acta*. **2013**, *112*, 159–163.
27. Wu, Y.Q.; Lu, G.X.; Li, S.B. The doping effect of Bi on TiO_2 for photocatalytic hydrogen generation and photodecolorization of rhodamine B. *J. Phys. Chem. C* **2009**, *113*, 9950–9955.
28. Villa, K.; Black, A.; Domenech, X.; Peral, J. Nitrogen doped TiO_2 for hydrogen production under visible light irradiation. *Solar Energy* **2012**, *86*, 558–566.
29. Naik, B.; Martha, S.; Parida, K.M. Facile fabrication of Bi_2O_3/$TiO_{2-x}N_x$ nanocomposites for excellent visible light driven photocatalytic hydrogen evolution. *Int. J. Hydrogen Energy* **2011**, *36*, 2794–2802.
30. Lin, H.; Shih, C.Y. Efficient one-pot microwave-assisted hydrothermal synthesis of M (M= Cr, Ni, Cu, Nb) and nitrogen co-doped TiO_2 for hydrogen production by photocatalytic water splitting. *J. Mol. Catal. A Chem*. **2016**, *411*, 128–137.
31. Sreethawong, T.; Laehsalee, S.; Chavadej, S. Comparative investigation of mesoporous-and non-mesoporous-assembled TiO_2 nanocrystals for photocatalytic H_2 production over N-doped TiO_2 under visible light irradiation. *Int. J. Hydrogen Energy* **2008**, *33*, 5947–5957.
32. Nagirnyi, V.; Feldbach, E.; Jönsson, L.; Kirm, M.; Kotlov, A.; Lushchik, A.; Nagornaya, L.L.; Savikhin, F.; Svensson, G. Study of oriented CdWO4 scintillating crystals using synchrotron radiation. *Radiat. Meas.* **2001**, *33*, 601–604.
33. Millers, D.; Grigorjeva, L.; Chernov, S.; Popov, A.; Lecoq, P.; Auffray, E. The temperature dependence of scintillation parameters in PbWO4 crystals. *Phys. Status Solidi B* **1997**, *203*, 585–589.
34. Lin, J.; Lin, J.; Zhu, Y.F. Controlled Synthesis of the $ZnWO_4$ Nanostructure and Effects on the Photocatalytic Performance. *Inorg. Chem*. **2007**, *46*, 8372−8378.
35. Shi, R.; Wang, Y.J.; Li, D.; Xu, J.; Zhu, Y.F. Synthesis of $ZnWO_4$ nanorods with [100] orientation and enhanced photocatalytic propertie. *Appl. Catal. B Environ*. **2010**, *100*, 173−178.
36. Zhao, X.; Zhu, Y.F. Synergetic degradation of rhodamine B at a porous $ZnWO_4$ film electrode by combined electro-oxidation and photocatalysis. *Environ. Sci. Technol*. **2006**, *40*, 3367−3372.
37. Mao, Y.; Wong, S.S. General, room-temperature method for the synthesis of isolated as well as arrays of single-crystalline ABO4-type nanorods. *J. Am. Chem. Soc*. **2004**, *126*, 15245–15252.
38. Li, Q.; Bai, X.X.; Luo, J.Y.; Li, C.Y.; Wang, Z.N.; Wu, W.W.; Liang, Y.P.; Zhao, Z.H. Fe doped $SrWO_4$ with tunable band structure for photocatalytic nitrogen fixation, *Nanotechnology* **2020**, *31*, 375402.
39. Trentelman, K.; Turner, C. Investigation of the painting materials and techniques of the late-15th century manuscript illuminator Jean Bourdichon. *J. Raman Spectrosc*. **2009**, *40*, 585–589.
40. Zhang, Q.; Zhou, Y.; Wang, F.; Dong, F.; Li, W.; Li, H.M.; Patzke, G.R. From semiconductors to semimetals: Bismuth as a photocatalyst for NO oxidation in air. *J. Mater. Chem. A* **2014**, *2*, 11065–11072.
41. Cheng, H.F.; Huang, B.B.; Lu, J.B.; Wang, Z.Y.; Xu, B.; Qin, X.Y.; Zhang, X.Y.; Dai, Y. Synergistic effect of crystal and electronic structures on the visible-light-driven photocatalytic performances of Bi_2O_3 polymorphs. *Phys. Chem. Chem. Phys*. **2010**, *12*, 15468–15475.
42. Zhao, Z.W.; Zhang, W.D.; Sun, Y.J.; Yu, J.Y.; Zhang, Y.X.; Wang, H.; Dong, F.; Wu, Z.B. Bi Cocatalyst/Bi_2MoO_6 Microspheres Nanohybrid with SPR-Promoted Visible-Light Photocatalysis. *J. Phys. Chem. C* **2016**, *120*, 11889–11898.
43. Li, F.; Zhao, W.; Leung, D.Y.C. Enhanced photoelectrocatalytic hydrogen production via Bi/$BiVO_4$ photoanode under visible light irradiation. *Appl. Catal. B Environ*. **2019**, *258*, 117954.
44. Tavakoli, F.; Salavati-Niasari, M.; Ghanbari, D.; Saberyan, K. Hosseinpour-Mashkani, S.M. Application of glucose as a green capping agent and reductant to fabricate CuI micro/nanostructures. *Mater. Res. Bull*. **2014**, *49*, 14–20.
45. Rather, R.A.; Sarwara, R.K.; Das, N.; Pal, B. Impact of reducing and capping agents on carbohydrates for the growth of Ag and Cu nanostructures and their antibacterial activities. *Particuology* **2019**, *43*, 219–226.
46. Li, X.Z.; Li, F.B. Study of Au/Au^{3+}-TiO_2 photocatalysts toward visible photooxidation for water and wastewater treatment. *Environ. Sci. Technol*. **2001**, *35*, 2381–2387.
47. Weng, S.X.; Chen, B.B.; Xie, L.Y.; Zheng, Z.Y.; Liu, P. Facile in situ synthesis of a Bi/BiOCl nanocomposite with high photocatalytic activity. *J. Mater. Chem. A* **2013**, *1*, 3068–3075.
48. Zhang, P.; Tachikawa, T.; Fujitsuka, M.; Majima, T. Efficient charge separation on 3D architectures of TiO_2 mesocrystals packed with a chemically exfoliated MoS_2 shell in synergetic hydrogen evolution. *Chem. Commun*. **2015**, *51*, 7187–7190.
49. Chen, X.B.; Shen, S.H.; Guo, L.J.; Mao, S.S. Semiconductor-based photocatalytic hydrogen generation. *Chem. Rev*. **2010**, *110*, 6503–6570.
50. Jeon, T.H.; Koo, M.S.; Kim, H.J.; Choi, W.Y. Dual-functional photocatalytic and photoelectrocatalytic systems for energy-and resource-recovering water treatment. *ACS Catal*. **2018**, *8*, 11542–11563.

51. Wei, Z.D.; Liu, J.Y.; Shangguan, W.F. A review on photocatalysis in antibiotic wastewater: Pollutant degradation and hydrogen production. *Chin. J. Catal.* **2020**, *41*, 1440–1450.
52. Chen, D.; Liu, Z.; Ouyang, S.X.; Ye, J.H. Simple room-temperature mineralization method to SrWO4 micro/nanostructures and their photocatalytic properties. *J. Phys. Chem. C* **2011**, *115*, 15778–15784.